

See discussions, stats, and author profiles for this publication at: <https://www.researchgate.net/publication/5494459>

# Combined Electron Magnetic Resonance and Density Functional Theory Study of 10 K X-Irradiated $\beta$ -D-Fructose Single Crystals

ARTICLE in THE JOURNAL OF PHYSICAL CHEMISTRY A · JUNE 2008

Impact Factor: 2.69 · DOI: 10.1021/jp7119284 · Source: PubMed

CITATIONS

16

READS

9

6 AUTHORS, INCLUDING:



**Einar Sagstuen**

University of Oslo

176 PUBLICATIONS 2,399 CITATIONS

SEE PROFILE



**Ewald Pauwels**

Ghent University

56 PUBLICATIONS 666 CITATIONS

SEE PROFILE



**Henk Vrielinck**

Ghent University

111 PUBLICATIONS 826 CITATIONS

SEE PROFILE



**Michel Waroquier**

Ghent University

417 PUBLICATIONS 8,263 CITATIONS

SEE PROFILE

# Combined Electron Magnetic Resonance and Density Functional Theory Study of 10 K X-Irradiated $\beta$ -D-Fructose Single Crystals

Mihaela Tarpan,<sup>†,\*</sup> Einar Sagstuen,<sup>§</sup> Ewald Pauwels,<sup>‡,#</sup> Henk Vrielinck,<sup>†,#</sup> Michel Waroquier,<sup>‡</sup> and Freddy Callens<sup>\*,†</sup>

Department of Solid State Sciences, Ghent University, Krijgslaan 281-S1, B-9000 Gent, Belgium, Center for Molecular Modeling, Ghent University, Proefuinststraat 86, B-9000 Gent, Belgium, and Department of Physics, University of Oslo, P.O. Box 1048 Blindern, N-0316 Oslo, Norway

Received: December 20, 2007; In Final Form: February 6, 2008

Primary free radical formations in fructose single crystals X-irradiated at 10 K were investigated at the same temperature using X-band Electron Paramagnetic Resonance (EPR), Electron Nuclear Double Resonance (ENDOR) and ENDOR induced EPR (EIE) techniques. ENDOR angular variations in the three principal crystallographic planes and a fourth skewed plane allowed the unambiguous determination of five proton hyperfine coupling tensors. From the EIE studies, these hyperfine interactions were assigned to three different radicals, labeled T1, T1\* and T2. For the T1 and T1\* radicals, the close similarity in hyperfine coupling tensors suggests that they are due to the same type of radical stabilized in two slightly different geometrical conformations. Periodic density functional theory calculations were used to aid the identification of the structure of the radiation-induced radicals. For the T1/T1\* radicals a C3 centered hydroxyalkyl radical model formed by a net H abstraction is proposed. The T2 radical is proposed to be a C5 centered hydroxyalkyl radical, formed by a net hydrogen abstraction. For both radicals, a very good agreement between calculated and experimental hyperfine coupling tensors was obtained.

## 1. Introduction

Considerable attention has been paid to the radiation chemistry of saccharides for a number of reasons. First, sugar radicals have a very important role in the radiation-induced damage of DNA, despite their relatively low abundance. Several years ago, Hole et al. identified at least nine sugar-centered radicals in 2'-deoxyguanosine 5'-monophosphate single crystals X-irradiated at 10 K.<sup>1</sup> One of these radicals is of particular interest because it appears to involve rupture of the phosphoester bond between C5' and O5' which, if formed in DNA, will lead to a prompt single-strand break. When the rupture is produced on both strands in proximity of each other, this can result in a lethal double-strand break.<sup>2</sup>

Second, the treatment of foodstuffs and pharmaceuticals using ionizing radiation, with the aim of improving the hygienic quality, has been common practice for a couple of decades.<sup>3</sup> From a safety and regulatory point of view, distinguishing between irradiated and nonirradiated food, and even the determination of the radiation dose, are major concerns. A number of studies are available that focus on the dosimetric characteristics of sugar systems.<sup>4,5</sup> Other studies, like the present one, are trying to understand the identity and the structural properties of the involved radicals, and the reactions evolving from the primary radical. For this purpose model systems, such as

glucose,<sup>6,7</sup> fructose,<sup>8,9</sup> sucrose<sup>10–12</sup> and rhamnose<sup>13–18</sup> single crystals have previously been experimentally investigated using Electron Paramagnetic Resonance (EPR), Electron Nuclear Double Resonance (ENDOR) spectroscopy and theoretically by means of Density Functional Theory (DFT) calculations.

An EPR/ENDOR study on room temperature (RT) X-irradiated  $\beta$ -D-fructose single crystals was published by Vanhaelewyn et al.<sup>8</sup> Two distinct stable radicals were identified, each of them characterized by three proton hyperfine couplings. The similarity of both principal values and principal directions for these two radicals indicates that the same type of radical probably occurs in two slightly different geometrical conformations. Pauwels et al.<sup>19</sup> presented a DFT study on the structure of the radiation-induced radicals in  $\beta$ -D-fructose single crystals observed at RT, using a single molecule approach. Four radical models were considered: two of the radical models formed by hydrogen abstraction from C5 and C4, the third model is formed by hydroxyl methyl group abstraction, with the unpaired spin mainly located on the C2 atom whereas a fourth model is obtained by removal of the hydroxyl group from the C2 carbon atom (see Figure 1 for the atomic numbering scheme). From these four radical models, it was concluded that only the last one yielded satisfactory agreement with the experimental data within the limits of the employed calculational method.

Very recently, Vanhaelewyn et al.<sup>9</sup> presented a detailed EPR/ENDOR and DFT study of  $\beta$ -D-fructose single crystals *in situ* X-irradiated at 80 K. The measurements revealed the presence of at least four carbon centered radicals. Two of them, labeled R1 and R1', exhibit only  $\beta$  proton hyperfine couplings, and the other two radicals, R2 and R3, are each characterized mainly by an  $\alpha$  coupling. For R1/R1', a radical model obtained by abstraction of a hydrogen from C3 was found to be in very good agreement with the experimental results. The other radicals

\* To whom correspondence should be addressed. Tel: +32 9 264 43 52. Fax: +32 9 264 49 96. E-mail: Freddy.Callens@ugent.be.

<sup>†</sup> Department of Solid State Sciences, Ghent University.

<sup>‡</sup> Research assistant of the Fund for Scientific Research—Flanders (Belgium) (F.W.O.—Vlaanderen).

<sup>§</sup> University of Oslo.

<sup>#</sup> Center for Molecular Modeling, Ghent University.

<sup>\*</sup> Postdoctoral Fellow of the Fund for Scientific Research—Flanders (Belgium) (F.W.O.—Vlaanderen).

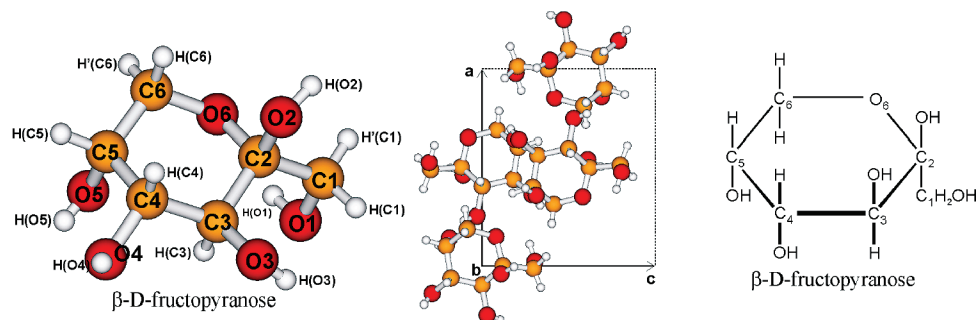


**Figure 1.** Left: molecular structure of  $\beta$ -D-fructose with labeled atoms. Central: four  $\beta$ -D-fructose molecules in the unit cell. Right: fructose chemical structure.

R2/R3 were suggested to be open ring species with a disrupted C2–C3 and a double C2–O2 bond. A possible formation mechanism for the open-ring species, starting from an alkoxy radical with the unpaired spin located on the O2 oxygen atom, was also presented.

When ionizing radiation interacts with matter, two main processes occur: excitation and ionization. In the ionization process the electrons are expelled from the atoms or molecules (oxidation), giving rise to paramagnetic molecules or molecular ions which can be studied using the EPR technique. The expelled electrons might have enough energy to produce secondary ionizations and excitations. When the kinetic energy of the electron has been largely dissipated, the electron attaches to another atom or molecule (reduction), again giving rise to paramagnetic molecular ions. At low temperatures the thermalized electron alternatively may become intermediately trapped in a polar lattice, e.g., because of a particular arrangement of the polarized OH groups, before eventually becoming captured by a neighboring molecule upon thermal annealing. Because the primary oxidation products, the reduction products and trapped electrons are highly unstable at room temperature, they can be observed only at very low temperatures. The irradiation process and the measurements are thus preferably carried out at very low temperatures without any annealing of the sample. Identifying the primary irradiation products is very important to test the proposed mechanisms for formations of the stable radicals. Therefore, the present study was carried out at 10 K, the lowest temperature for *in situ* irradiation available in our laboratories.

During the past few years, it has become more and more common to complement EPR/ENDOR experiments by DFT calculations. This *ab initio* technique allows the optimization of a tentative radical structure and the calculation of spin Hamiltonian parameters. By then, comparing calculated with measured hyperfine coupling tensors, one can assess the validity of the proposed radical model. This approach has been used in the current work to examine several radical models for the low-temperature radiation induced defects in fructose single crystals.

## 2. Materials and Methods

Single crystals of  $\beta$ -D-fructose (Sigma-Aldrich) were grown from saturated aqueous solutions containing ethanol by slow evaporation at 40 °C. It has not been possible to produce satisfactory crystals of partially deuterated  $\beta$ -D-fructose from deuterated solvents.  $\beta$ -D-fructose crystals are orthorhombic with space group symmetry  $P2_12_12_1$  and four molecules in the unit cell (Figure 1).<sup>20,21</sup> The crystal axes were labeled according to a neutron diffraction study,<sup>21</sup> i.e.  $a = 0.9191$  nm,  $b = 1.0046$  nm and  $c = 0.8095$  nm.  $\langle a \rangle$ ,  $\langle b \rangle$  and  $\langle c \rangle$  were chosen as the reference axes for the Electron Magnetic Resonance (EMR) experiments.

For the identification of the crystal axes, single crystals of  $\beta$ -D-fructose were mounted onto a goniometer head of a Weissenberg X-ray diffraction camera. Using oscillation diagrams, the rotation axis was aligned within 1° along one of the crystal axes to be used as the crystal rotation axis in the EMR experiment except for the case of recording data in a skew plane (see below). The crystals were then transferred and glued to copper sample holders without loss of alignment. The copper crystal holder is mounted to an Air Products HeliTran LT3-110 cryostat cooled by liquid helium. The cryostat was inserted into the telescopic cryostat holder of the EPR/ENDOR setup at the University of Oslo, specially designed for low-temperature *in situ* X-irradiation. The position of the crystal was adjusted to the same height as the irradiation window. Before irradiation the crystal holder and the sample were cooled to about 10 K. A Philips chromium-anode X-ray tube operated at 60 kV and 40 mA was used for the irradiation and an estimated dose of about 40 kGy was delivered to the crystal. After irradiation the sample was, without annealing, lowered in the TM<sub>011</sub> cylindrical resonance cavity for the low-temperature measurements.

The X-band (around 9.5 GHz) EMR measurements were performed at the University of Oslo using a BRUKER ELEX-SYS 560 SuperX spectrometer connected to a Linux workstation. For the ENDOR and EIE measurements an ENI 3200L RF power amplifier was used. The EPR and ENDOR measurements were performed in four different rotation planes, the three principal crystallographic planes ( $\langle ab \rangle$ ,  $\langle ac \rangle$  and  $\langle bc \rangle$  planes) and a fourth skewed plane ( $\theta = 52^\circ$ ;  $\varphi = 90^\circ$ ), by rotating the sample in 5° steps over 100°. The measurements in the skewed plane were required to solve the Schonland ambiguity.<sup>22</sup> The EIE measurements were performed with the magnetic field along the crystallographic axes and helped to assign the various ENDOR lines to particular radicals. To determine the proton hyperfine coupling tensors from the ENDOR angular variations, the MAGRES<sup>23</sup> program was used.

## 3. Computational Details

All calculations were performed with the Quickstep code,<sup>24</sup> which is part of the freely available program package CP2K.<sup>25</sup> The gradient-corrected exchange-correlation BLYP density functional<sup>26</sup> was used throughout. The fructose crystal phase was simulated under periodic boundary conditions, fully exploiting the translational symmetry of the crystal. A supercell was constructed by doubling the crystallographic unit cell in the  $\langle c \rangle$  direction. One of the resulting 8 molecules was then transformed into an initial radical structure by removing a hydrogen atom. The supercell approach is essential in periodic calculations because it ensures that radical defects in adjacent cells are well separated from each other.

The structure of each radical model was optimized with the Gaussian and plane waves method (GPW),<sup>27</sup> which employs

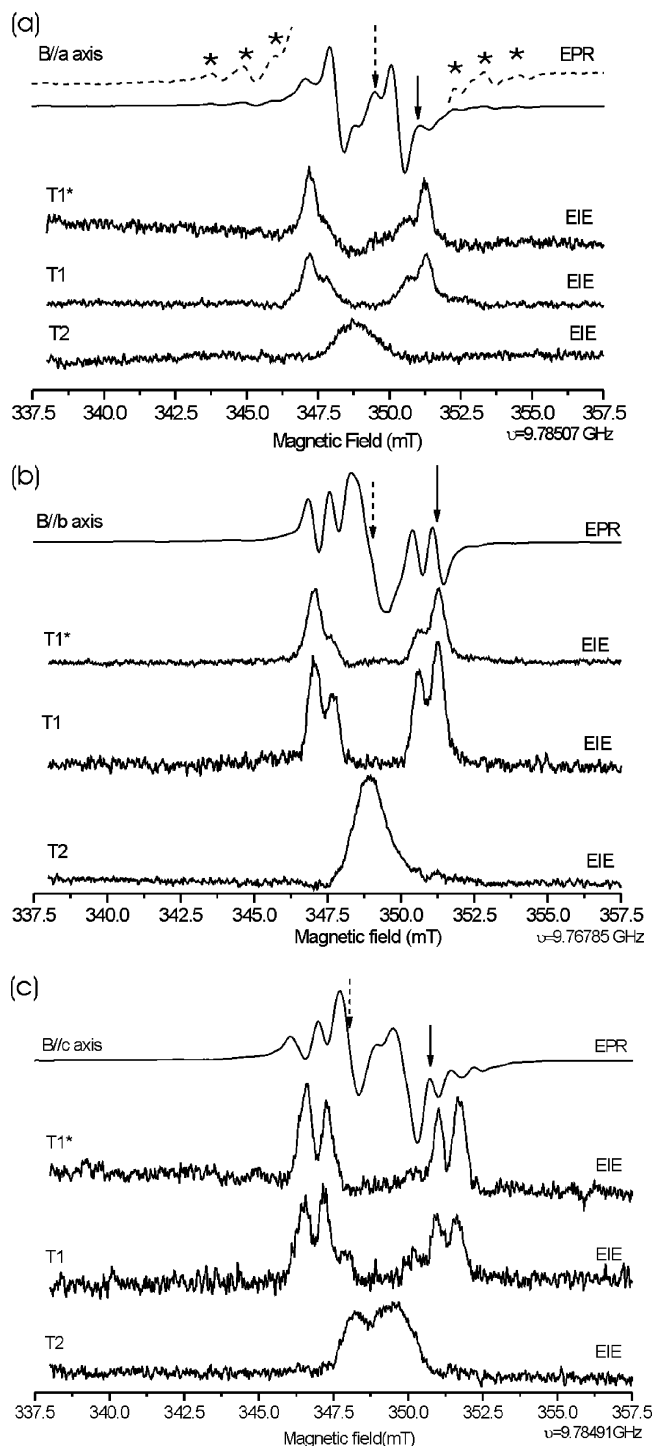


**Figure 2.** X-band EPR and EIE spectra from fructose single crystals X-irradiated at 10 K for the magnetic field along the three crystallographic axes. The ENDOR spectra were obtained with the magnetic field position locked to the EPR lines marked by arrows. In Figure 2a the EPR spectrum is accompanied by a 5 times amplified version for a better view of the wing lines, marked by stars.

Gaussian-type atom-centered basis functions to describe the wave functions and an auxiliary plane wave basis to describe the density. Goedecker–Teter–Hutter (GTH) type pseudopotential<sup>28</sup> were applied at a 400 Ry cutoff along with matching Gaussian basis sets of triple-valence quality (TZVP-GTH).<sup>24,29</sup> The dimensions of the supercell were kept constant during these calculations, but no constraints were imposed on the individual atoms.

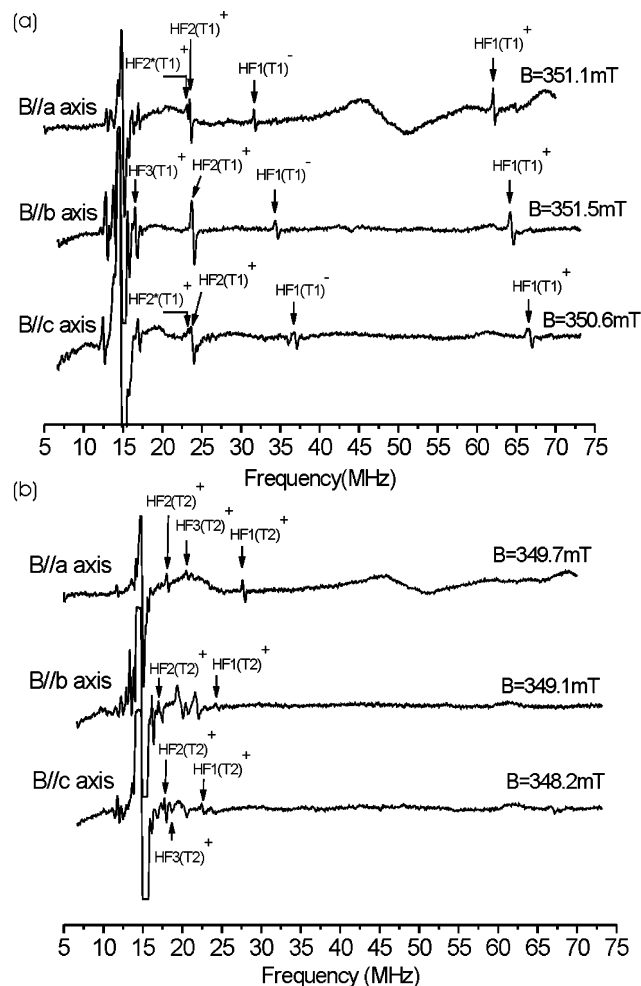


**Figure 3.** X-band ENDOR spectra from fructose single crystals X-irradiated at 10 K for the magnetic field along the three crystallographic axes. At each axis orientation, the magnetic field was locked at two different positions in EPR spectrum, as indicated. The high- and low-frequency ENDOR lines are indicated with superscripts + and −, respectively. (a) ENDOR spectra associated with the T1/T1\* radical. (b) ENDOR spectra associated with the T2 radical.

Subsequent to optimization, hyperfine coupling tensors were determined on the entire supercell containing the radical. This was done with a recently introduced method<sup>30</sup> that relies on an all-electron implementation of the Gaussian and Augmented Plane waves (GAPW) scheme.<sup>31</sup> The main benefit of the latter over GPW is that a density reconstruction scheme ensures a superior description of the density localized close to the nuclei. This is less important for the determination of optimum geometries but is crucial when hyperfine coupling tensors are to be calculated. An all-electron variant of the TZVP basis set was used<sup>32</sup> and the density cutoff for the auxiliary plane wave basis set was again set to 400 Ry. This AE-GAPW implementation was recently shown to very accurately calculate hyperfine coupling tensors of sugar<sup>33</sup> or amino-acid radicals.<sup>30</sup>

#### 4. Experimental Results

**4.1. EPR of  $\beta$ -D-Fructose Single Crystals.** All EPR, ENDOR and EIE measurements presented in this study were carried out at 10 K. A typical EPR spectrum consists of many strongly overlapping broad resonances lines in the central region (about 8 mT around  $g = g_e$ ; see Figures 2a–c) together with some weaker lines on each side (marked by stars in the amplified EPR spectrum Figure 2a). The average intensity of the latter



**TABLE 1: Experimental Proton Hyperfine Coupling Tensors (MHz) Obtained from X-Band ENDOR Measurements at 10 K Using Fructose Single Crystals X-Irradiated at 10 K<sup>a</sup>**

radical	tensor	principal values	isotropic values	anisotropic values	principal directions		
					<i>a</i>	<i>b</i>	<i>c</i>
T1	HF1(T1)	106.26(3)	99.31(2)	6.95(4)	0.010(1)	0.497(8)	0.868(3)
		97.53(3)		−1.79(4)	−0.355(1)	0.810(3)	−0.467(7)
		94.16(3)		−5.16(4)	−0.935(1)	−0.313(2)	0.168(3)
	HF2(T1)	23.52(3)	17.80(2)	5.72(4)	0.506(2)	−0.592(1)	−0.627(12)
		15.43(4)		−2.38(4)	0.613(3)	0.758(7)	−0.221(17)
		14.46(2)		−3.34(3)	0.607(2)	−0.272(2)	0.747(4)
T1*	HF2(T1*)	22.75(3)	17.40(2)	5.35(4)	0.494(3)	−0.573(11)	−0.654(5)
		15.57(3)		−1.83(4)	0.461(2)	0.810(3)	−0.361(11)
		13.89(4)		−3.52(4)	0.737(2)	−0.123(7)	0.665(4)
T2	HF1(T2)	30.14(2)	19.78(2)	10.36(3)	0.836(1)	−0.547(7)	−0.052(4)
		15.67(5)		−4.11(5)	0.258(1)	0.308(9)	0.916(3)
		13.53(3)		−6.25(4)	0.485(2)	0.779(5)	−0.398(11)
	HF2(T2)	7.94(6)	6.26(3)	1.68(7)	0.482(12)	0.077(7)	−0.873(25)
		6.15(5)		−0.12(6)	0.875(15)	0.005(27)	0.484(1)
		4.71(4)		−1.56(5)	0.042(6)	−0.997(12)	−0.064(18)

<sup>a</sup> The numbers in parentheses represent the uncertainty in the last significant digit(s).

lines is about 2 orders of magnitude smaller than that of the largest central resonances.

The central part of the X-band EPR spectra shows only weak anisotropy. Hence, the *g*-tensor of the involved radicals was assumed to be isotropic for the further analysis of the hyperfine coupling tensors. The weak resonance lines on each side of the central region (Figure 2a) also exhibit very small *g* anisotropy which leads to the conclusion that they are not related to alkoxy radicals. Indeed, paramagnetic absorption of alkoxy radicals is characterized by considerable *g* shifts arising from spin–orbit coupling of the unpaired electron localized primarily on the oxygen atom.<sup>34,35</sup>

The EPR angular variation did not allow an accurate interpretation of the spectra, and unfortunately ENDOR measurements for the weak flanking lines were not successful probably due to the low intensity of the EPR signals. Therefore, the results presented below are limited to the resonances of the central part of the spectrum.

#### 4.2. ENDOR and EIE of $\beta$ -D-Fructose Single Crystals.

After X-irradiation and measurements at 10 K, five hyperfine coupling tensors could be determined from the ENDOR angular variations in the four planes mentioned above (Table 1). In Figure 3, typical ENDOR spectra for the magnetic field along the  $\langle a \rangle$ ,  $\langle b \rangle$  and  $\langle c \rangle$  axes are shown. Along each axis, the ENDOR spectra were recorded for two different magnetic field values in the EPR spectrum to obtain all the relevant resonance lines. In Figure 3a, the ENDOR lines obtained with the magnetic field position locked to the EPR lines marked by solid arrows in Figure 2, are shown. From the angular variation of these lines the hyperfine coupling tensors labeled HF1(T1), HF2(T1) and HF2(T1\*) were obtained. The hyperfine coupling tensors labeled HF1(T2) and HF2(T2) were obtained with the magnetic field locked to one of the central EPR lines (marked by dashed arrows in Figure 2). The corresponding ENDOR lines are shown in Figure 3b. In Figure 4 the angular dependence of all assigned ENDOR lines is shown.

By using EIE, it was demonstrated that three radicals are responsible for these five proton interactions. The radical denoted T1 exhibits three  $\beta$ -proton hyperfine couplings: a large coupling, HF1(T1), around 100 MHz, a smaller coupling, HF2(T1), around 20 MHz and a third, relatively small coupling, labeled HF3(T1). Only the HF1(T1) and HF2(T1) hyperfine

coupling tensors could be completely determined from the ENDOR angular variations. The third interaction could only be followed in the *bc* plane which is not sufficient for an accurate determination of the hyperfine coupling tensor. However, when EIE was performed on any of the ENDOR lines HF1(T1), HF2(T1) and HF3(T1) for the magnetic field along the *b*-axis (Figure 3a), similar EIE spectra (labeled T1 in Figure 2b) were observed. For the magnetic field along the  $\langle a \rangle$  and  $\langle c \rangle$  axes, satisfactory EIE spectra were obtained only for the HF1(T1) and HF2(T1) ENDOR lines (Figures 2a and 2c).

In all four rotation planes both the HF1(T1) and HF2(T1) ENDOR lines are closely accompanied by resonance lines of other virtually identical couplings, but only the HF2(T1\*) hyperfine coupling tensor could be determined. The similarity of the hyperfine coupling tensors HF2(T1) and HF2(T1\*) suggests that they originate from the same type of radical in two slightly different geometrical conformations, as often occurs in these kind of crystals.<sup>8,9,12</sup>

The second radical, denoted T2, exhibits only smaller hyperfine couplings, with isotropic values in the range 5–20

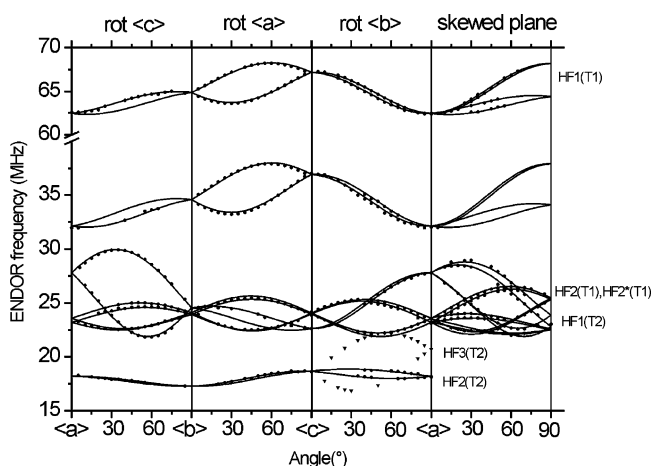


**Figure 4.** ENDOR line angular variation in all three principal planes and in the skewed plane. The solid circles represent the experimental points for the five interactions for which proton hyperfine coupling tensors were determined and the solid lines through the circles are the simulations using the data in Table 1. The triangles “▼” represent the experimental points for the HF3(T2) ENDOR lines in the  $\langle ac \rangle$  plane.

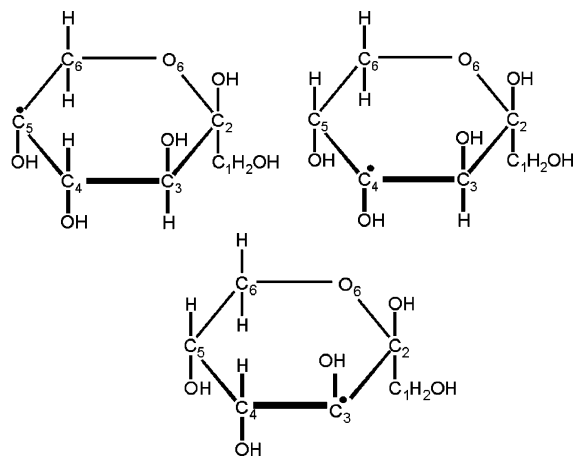


**Figure 5.** C5 (upper left), C4 (upper right) and C3-centered (bottom) fructose radical model

MHz. From the EIE measurements at least three different proton interactions that could be assigned to this radical were observed, but only two hyperfine coupling tensors could be completely determined: HF1(T2) and HF2(T2). For the third proton interaction, labeled HF3(T2), ENDOR lines could only be followed in the  $\langle ac \rangle$  plane, which did not allow for a complete determination of the hyperfine coupling tensor. In Figure 4, the ENDOR line positions of HF3(T2) in the  $\langle ac \rangle$  plane are shown as triangles, together with the line positions of the well resolved ENDOR lines in all four rotation planes, shown as solid circles.

Performing EIE measurements on the ENDOR lines HF1(T2) and HF2(T2) resulted in similar EIE spectra (labeled T2 in Figure 2) for the magnetic field along each of the three crystallographic axes. For the magnetic field along the  $\langle c \rangle$  axis, the EIE spectrum for radical T2 could only be recorded for the HF2(T2) ENDOR line and the signal is not a broad singlet as for the other two orientations but appears to exhibit an additional splitting. Most likely this additional splitting is not real but originates from an EIE contribution from another radical. This is a common problem for the ENDOR lines close to the proton Larmor frequency, because of partial or even fully overlapping of the resonance lines.

## 5. Radical Model Assignments

After X-irradiation of  $\beta$ -D-fructose single crystals at 10 K, three distinct radicals labeled T1, T1\* and T2 were characterized. These radical species may *a priori* be expected to be primary radiation products or species closely related to the primary products, in view of the low temperature used for the experiment. Therefore, in assigning models for these radicals, structures formed by simple processes, like net hydrogen abstractions from the pristine  $\beta$ -D-fructose molecule, were inspected first. Realizing that the T1, T1\* and T2 radicals exhibit interactions only with  $\beta$  protons, the three radical structures shown in Figure 5 appeared as the most promising candidate models. The three structures, denoted F(C3), F(C4) and F(C5), are all presumed to be formed by net hydrogen abstraction from C3, C4 and C5 respectively.

**5.1. Radical Models for T1/T1\*.** The F(C3) structure was previously proposed by Vanhaelewyn et al.<sup>7</sup> as the basic model for both the R1 and R1' radicals observed after X-irradiation at 80 K, an interpretation convincingly supported by cluster DFT calculations. A comparison of the present T1/T1\* tensors in Table 1 with those determined by Vanhaelewyn et al.<sup>7</sup> (reproduced in Table 2) yields an exceptionally good agreement between HF1(T1) and HF2(T1) from the present work and the

HF1( $\beta$ 1) and HF2( $\gamma$ 2) coupling tensors respectively of R1/R1' the previous work of Vanhaelewyn et al.<sup>7</sup> On the other hand, the present HF2(T1\*) tensor and the HF3, HF4, HF( $\beta$ 1') tensors from ref 7 do not seem to have any counterparts. Thus, even if the close similarity of the two strongest interactions, which were those used for the comparison with the DFT calculations, strongly suggests that the basic model for the T1/T1\* radicals is also the F(C3) structure, there are discrepancies in the number of  $^1\text{H}$  interactions, which are well reflected in the EIE spectra (for the Q-band EIE spectra after X-irradiation at 80 K, to be further discussed below, see Figure 3 in ref 7). This leads to the conclusion that T1 (T1\*) is closely related but still somehow different from R1 (R1'). The precise differentiation between the four radicals is, however, not obvious.

The hyperfine coupling tensors of the optimized F(C3) model were recalculated using the periodic GAPW approach (Table 3). Minor changes occurred with respect to the cluster DFT results published earlier,<sup>7</sup> apart from the isotropic H(C4) coupling which increased to 96.65 MHz. As is clear from Table 2, the H(C4) and H(O2) hyperfine tensors agree very well with HF1(T1) and HF2(T1) with respect to both the (an)isotropic couplings and the principal directions. The latter is visualized by the small angles ( $\delta$ ) between corresponding experimental and calculated eigenvectors. Furthermore, the predicted H(O3) coupling could account for the HF3(T1) signal, for which an experimental tensor could not be determined.

Because the F(C3) model seems to fit the T1/T1\* radicals (at 10 K) and the R1/R1' species (at 80 K) equally well, it may be argued that an alternative model structure exists for which the hyperfine parameters show a preferential agreement with either radical. In this respect, the similar F(C4) structure is a viable candidate, as was already contended in reference 7. The crystallographic C4...H(C3) direction in this model is comparable to the C3...H(C4) direction in F(C3) and so it can be expected that at least the H(C3) eigenvector for the maximum anisotropic component will be in equally good agreement with experiment as is the corresponding H(C4) eigenvector in F(C3). Periodic DFT calculations indicate that the radical model F(C4) has four protons with substantial hyperfine couplings (Table 3). There is a large proton hyperfine coupling around 100 MHz (H(C3)) along with one medium proton hyperfine coupling (H(O4)) and two relatively small couplings (H(C5) and H'(C6)). As anticipated, the hyperfine coupling tensor for the large coupling agrees quite well with HF1(T1). However, the hyperfine coupling tensor of the intermediate-sized coupling cannot reasonably be linked with T1/T1\*. Neither the isotropic nor the anisotropic components of the calculated H(O4) coupling, or any of the other predicted tensors, are close to the experimental HF2(T1) tensor. On this basis, model F(C4) has been rejected.

**5.2. Radical Model for T2.** From Table 3 it is also easily concluded that neither F(C4) nor F(C3) is a suitable candidate for the T2 radical, because the latter exhibits only small proton hyperfine couplings. The calculated EPR properties for the F(C5) model, however, are consistent with this requirement. From Table 4, it appears that this structure is characterized by six rather small hyperfine coupling tensors. One coupling exhibits an isotropic value of around 20 MHz (H(C4)), another is close to 12 MHz (H(C6)) and four nearly isotropic couplings are smaller than 10 MHz (H'(C6), H(O3), H(O5) and H(C1)). In Table 4, the DFT-calculated proton hyperfine coupling tensors for radical model F(C5) are compared with the experimental tensors for radical T2 in Table 1.

Comparing these calculated hyperfine coupling tensors with the experimental tensors for radical T2, one can notice that the

**TABLE 2: Experimental Proton Hyperfine Coupling Tensors (MHz) Obtained from Q-Band ENDOR Measurements at 80 K Using Fructose Single Crystals X-Irradiated at 80 K<sup>a</sup>**

radical	tensor	principal values	isotropic values	anisotropic values	principal directions		
					<i>a</i>	<i>b</i>	<i>c</i>
R1	$\vec{A}_{\text{HF1}(b1)}$	106.40	99.41	7.00	−0.0706	0.4709	0.8794
		97.42		−1.99	−0.1536	−0.8762	0.4569
		94.40		−5.01	−0.9856	0.1028	−0.1342
	$\vec{A}_{\text{HF2}(g2)}$	23.49	17.63	5.86	0.4795	−0.6227	0.6183
		15.35		−2.29	0.4971	0.7734	0.3934
		14.06		−3.57	0.7232	−0.1187	−0.6804
	$\vec{A}_{\text{HF3}}$	11.12 (B//a)	≈18.5				
		19.68 (B//b)					
		24.67 (B//c)					
	$\vec{A}_{\text{HF4}}$	21.41	11.42	10.00	0.1222	0.9912	−0.0511
		7.03		−4.39	0.7194	−0.0530	0.6926
		5.81		−5.61	0.6838	−0.1214	−0.7195
R1'	$\vec{A}_{b1e}$	105.53	98.58	6.95	−0.0795	0.4573	0.8858
		96.70		−1.87	−0.2143	−0.8757	0.4328
		93.50		−5.08	−0.9735	0.1554	−0.1676
R2	$\vec{A}_{\alpha 1}$	−9.86	−38.88	29.03	0.1643	0.9312	−0.3253
		−35.26		3.63	0.6102	−0.3550	−0.7083
		−71.54		−32.65	−0.7751	−0.0821	−0.6265
R3	$\vec{A}_{\alpha 2}$	−12.64	−45.59	32.94	0.3149	0.8774	−0.3619
		−43.92		1.66	0.5457	−0.4793	−0.6873
		−80.19		−34.60	−0.7765	−0.0189	−0.6298

<sup>a</sup> These data are reproduced from ref 7.**TABLE 3: Proton Hyperfine Coupling Tensors (MHz) from Periodic DFT Calculation for F(C3) and F(C4) Radical Models<sup>a</sup>**

radical	tensor	isotropic values	anisotropic values	principal directions			$\delta$ (deg)
				<i>a</i>	<i>b</i>	<i>c</i>	
F(C3)	H(C4)	96.65	6.60	0.065	0.539	0.840	4
			−1.79	−0.166	0.835	−0.524	11
			−4.82	−0.984	−0.105	0.144	12
	H(O2)	18.94	5.76	0.490	−0.619	−0.613	2
			−2.02	0.567	0.761	−0.315	6
			−3.75	0.662	−0.194	0.724	6
	H(O3)	8.45	19.95	−0.469	−0.111	−0.876	
			−8.78	0.517	−0.839	−0.170	
			−11.17	−0.716	−0.533	0.451	
F(C4)	H(C3)	102.87	6.36	0.121	0.599	0.792	10
			−0.81	−0.545	0.707	−0.451	12
			−5.54	−0.830	−0.377	0.412	16
	H(O4)	45.61	21.50	0.963	−0.113	−0.245	45
			−9.22	−0.052	0.812	−0.581	45
			−12.28	0.265	0.573	0.776	54
	H(C5)	8.29	9.26	0.839	0.001	0.543	
			−3.60	−0.142	0.966	0.217	
			−5.66	−0.525	−0.259	0.811	
	H'(C6)	7.84	3.72	0.988	0.121	−0.091	
			−1.53	0.139	−0.965	0.222	
			−2.19	0.061	0.233	0.971	

<sup>a</sup>  $\delta$  (deg) are the angles between the principal directions of the experimental tensors for the T1 radical and the calculated tensors.

H(C4) tensor is in very good agreement with HF1(T2). The deviations ( $\delta$ ) between the principal directions of the calculated and experimental eigenvectors are less than 11° and the isotropic and anisotropic components are matching the experimental values excellently. The EIE measurements revealed that at least two other proton interactions (of smaller magnitude) are present for the radical, but only the HF2(T2) hyperfine coupling tensor

**TABLE 4: Proton Hyperfine Coupling Tensors (MHz) from Periodic DFT Calculation for the F(C5) Radical Model<sup>a</sup>**

radical	tensor	isotropic values	anisotropic values	principal directions			$\delta$ (deg)
				<i>a</i>	<i>b</i>	<i>c</i>	
F(C5)	H(C4)	20.69	10.35	0.829	−0.559	0.002	3
			−4.44	0.313	0.467	0.827	11
			−5.91	0.464	0.685	−0.562	11
	H(C6)	11.87	9.34	0.339	0.851	−0.401	
			−3.35	0.291	0.310	0.905	
			−5.98	0.895	−0.424	−0.142	
	H'(C6)	4.96	9.08	0.845	0.284	−0.453	
			−3.68	0.391	0.251	0.886	
			−5.40	0.365	−0.925	0.101	
	H(O3)	7.94	1.80	0.749	0.197	−0.633	22
			−0.32	0.623	−0.537	0.569	35
			−1.49	−0.228	−0.820	−0.524	35
	H(O5)	7.12	20.20	0.425	0.789	−0.444	
			−9.12	−0.206	0.561	0.802	
			−11.09	0.882	−0.249	0.401	
	H(C1)	1.87	1.25	0.484	0.028	−0.874	3
			−0.36	0.875	0.013	0.485	0
			−0.89	0.025	−1.000	−0.018	3

<sup>a</sup>  $\delta$  (deg) are the angles between the principal directions of the experimental tensors from the T2 radical and the calculated tensors: H4 is compared with HF1(T2), HO3 and H1 with HF2(T2).

could be determined unambiguously. The predicted H(O3) tensor as well as that for H(C1) qualitatively succeed in reproducing the measured anisotropy of HF2(T2). The H1 tensor exhibits principal directions that are within 3° from their experimental counterparts, but the isotropic hyperfine coupling is far smaller than the experimental value. On the other hand, the H(O3) coupling is in magnitude much closer to the HF2-(T2) coupling, whereas the deviations between the principal directions are larger.

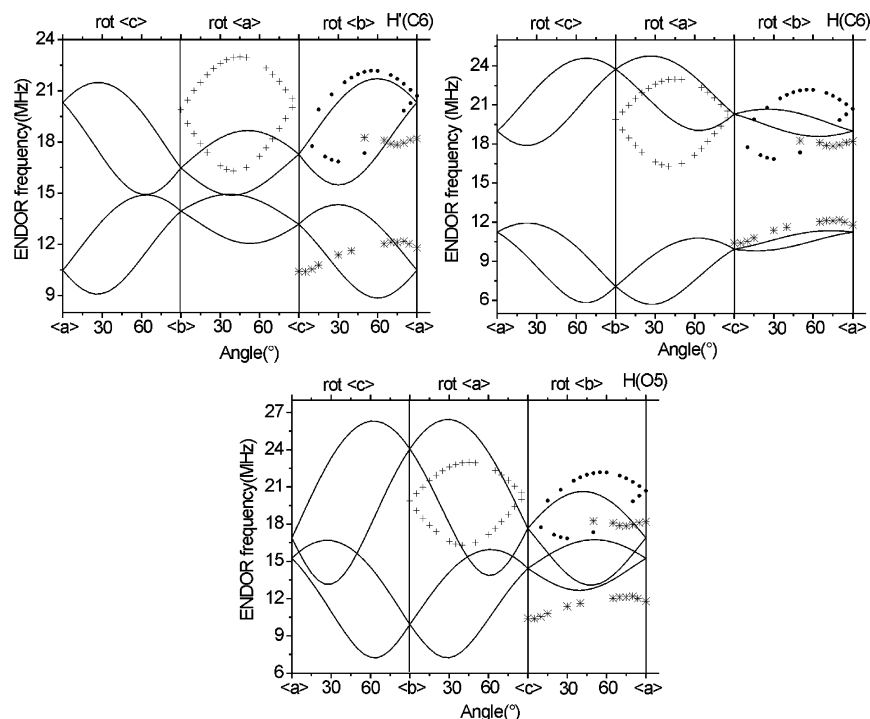


**Figure 6.** Comparison between the simulated  $H'(C6)$ ,  $H(C6)$  and  $H(O5)$  proton hyperfine coupling from radical model  $F(C5)$  (solid lines) and the experimental hyperfine couplings:  $HF3(T2)$  (dots),  $Int1$  (crosses) and  $Int2$  (stars).

However, given the computational uncertainty for small couplings together with the inherently large uncertainties associated with the experimentally determined eigenvectors of nearly isotropic couplings it is difficult to make an assignment of the  $HF2(T2)$  tensor to either of these nuclei. The  $H(O3)$  tensor can be slightly favored because the  $\alpha$ -like orthorhombic symmetry of the dipolar tensor part is most successfully reproduced in the calculations. Furthermore, supplementary calculations indicate that only a slight reorientation of the  $H(O3)$ — $O3$  hydroxyl group is sufficient to reduce the difference between calculated and experimental principal directions below  $20^\circ$ .

In addition to the  $HF3(T2)$  coupling, two other proton hyperfine couplings, labeled  $Int1$  and  $Int2$ , were clearly noticed in the ENDOR spectra. Again, no hyperfine coupling tensors could be obtained because the corresponding resonances could be followed only in one rotational plane ( $Int1$  in the  $\langle bc \rangle$  plane and  $Int2$  in the  $\langle ac \rangle$  plane) and also, no EIE spectra could be recorded for them.

To check whether these couplings also arise from the  $T2$  radical, they were compared with the unassigned calculated tensors from the  $F(C5)$  radical model:  $H(C6)$ ,  $H'(C6)$  and  $H(O5)$ . Figure 6 shows the experimentally ENDOR line positions for couplings  $HF3(T2)$ ,  $Int1$  and  $Int2$  together with the simulated ENDOR line variations calculated from the  $H(C6)$ ,  $H'(C6)$  and  $H(O5)$  hyperfine coupling tensors, respectively, in Table 4. The simulation for the hyperfine coupling tensor  $H(C6)$  (Table 4) reproduces reasonably well the  $Int2$  ENDOR line angular variation in the  $\langle ac \rangle$  plane, with a difference of about 1 MHz in isotropic component. The simulations for the hyperfine coupling tensor  $H'(C6)$  (Table 4) carries some similarity with the  $HF3(T2)$  hyperfine coupling, although not as convincing as for  $Int2$  vs  $H(C6)$ . The simulation for the  $H(O5)$  calculated tensor cannot be correlated with either the  $Int1$  hyperfine coupling or with any other experimental interaction. Thus it is possible that the interaction  $Int2$  can be assigned to radical  $T2$  and interaction  $Int1$  may be due to a minority fourth radical for which further information is not available.

## 6. Discussion and Conclusions

Five proton hyperfine coupling tensors, assigned to three radicals labeled  $T1$ ,  $T1^*$  and  $T2$ , could be determined from ENDOR angular variations in four rotation planes. Radical models were proposed for each of these radicals and very good agreement was found between the experimentally available and DFT-calculated hyperfine coupling tensors. For the  $T1/T1^*$  radical a  $C3$  centered model formed by a net  $H(C3)$  abstraction is proposed. The  $T2$  radical is identified as a  $C5$  centered radical, again formed by a net hydrogen atom ( $H(C5)$ ) abstraction.

As already mentioned above, the  $T1/T1^*$  (10 K) and  $R1/R1^*$  (80 K) radicals seem to be closely related, the mutual differences of the corresponding tensors being even smaller than the small discrepancies between, e.g., the experimental values for  $T1$  and the DFT-calculated ones. However, it has also been emphasized that at both temperatures coupling tensors without counterparts are present. The difference between the 10 and 80 K radicals can be best seen in the EIE spectra of the  $T1$  (Figure 2) and  $R1$  (ref 7, Figure 3) radicals for the magnetic field along the crystallographic axes. The EIE spectra of radical  $T1$  are characterized by a doublet of doublets for the magnetic field along the  $\langle a \rangle$  and  $\langle b \rangle$  axes. For the  $R1$  radical, the EIE spectrum for  $B//\langle a \rangle$  is a broad doublet, and for  $B//\langle b \rangle$  a doublet of quadruplets is observed. For  $B//\langle c \rangle$  a doublet of triplets is observed in both cases. This demonstrates that the difference between the  $T1$  and  $R1$  radicals must be due to a change in the number of coupling nuclei and/or a change in coupling strength of certain proton interactions as a consequence of differences in radical geometry or chemical structure. These differences apparently occur in a part of the radical structure that has only negligible influence on the  $HF(H(C4))$  and  $HF(H(O2))$  interactions. Differences in geometrical conformations have also previously been the basis for explaining small differences between two or more similar radicals (see, e.g., glucose, sorbose and sucrose<sup>6,7,10</sup>). It is clear, however, that at the present state



of experimental and theoretical knowledge about the radicals in fructose, the origins for these differences cannot be further detailed.

Pulse anneal experiments are underway in our laboratories to study the transformation of the T1/T1\* into the R1/R1\* signals/radicals. For this purpose,  $\beta$ -D-fructose crystals, X-irradiated at 10 K, will be warmed up for several minutes at a few intermediate temperatures between 10 and 80 K, and subsequently recooled and measured using EPR, ENDOR and EIE at 10 K. Such experiments may also clarify how the T2 radical evolves as it seems to be absent after irradiation at 80 K. Concomitantly, systematic DFT studies of geometrical conformations of the same radicals will be carried out.

**Acknowledgment.** We acknowledge the Fund for Scientific Research-Flanders (Belgium) (F.W.O.—Vlaanderen) and the COST P15 for the financial support concerning the stay at the University of Oslo.

## References and Notes

- (1) Hole, E. O.; Nelson, W. H.; Sagstuen, E.; Close, D. M. *Radiat. Res.* **1992**, *129*, 119.
- (2) Sevilla, M. D.; Becker, D. *ESR Studies of Radiation Damage to DNA and Related Biomolecules. Chapter 6 in Electron Paramagnetic Resonance: Volume 19; Series: Specialist Periodical Reports* 2004.
- (3) Diehl, J. F. *Safety of Irradiated Foods*, Marcel Dekker, New York 1995.
- (4) Nakajima, T.; Otsuki, T.; Hara, H.; Nishiwaki, Y.; Matsuo, M. *Radiat. Prot. Dosim.* **1990**, *34*, 303.
- (5) Yordanov, N. D.; Georgieva, E. *Spectrochim. Acta A* **2004**, *60*, 1307.
- (6) Madden, K. P.; Bernhard, W. A. *J. Phys. Chem.* **1979**, *83* (20), 2643.
- (7) Pauwels, E.; Van Speybroeck, V.; Callens, F.; Waroquier, M. *Int. J. Quantum Chem.* **2004**, *99* (2), 102.
- (8) Vanhaelewyn, G. C. A. M.; Lahorte, P. G. A.; De Proft, F. J. A.; Geerlings, P. F. C.; Mondelaers, W. K. P. G.; Callens, F. J. *Phys. Chem. Chem. Phys.* **2001**, *3* (9), 1709.
- (9) Vanhaelewyn, G. C. A. M.; Pauwels, E.; Callens, F. J.; Waroquier, M.; Sagstuen, E.; Matthys, P. *J. Phys. Chem. A* **2006**, *110*, 2147.
- (10) Sagstuen, E.; Lund, A.; Awadelkarim, O.; Lindgren, M.; Westerling, J. *J. Phys. Chem.* **1986**, *90*, 5584.
- (11) Vanhaelewyn, G.; Sadlo, J.; Callens, F.; Mondelaers, W.; De Frenne, D.; Matthys, P. *Appl. Radiat. Isot.* **2000**, *52*, 1221.
- (12) De Cooman, H.; Pauwels, E.; Vrielinck, H.; Dimitrova, A.; Yordanov, N.; Sagstuen, E.; Waroquier, M.; Callens, F. *Spectrochim. Acta A*, in press, doi:10.1016/j.saa.2007.09.033.
- (13) Box, H. C.; Budzinski, E. E.; Freund, H. G. *J. Chem. Phys.* **1990**, *121*, 262.
- (14) Samskog, P. O.; Lund, A.; Nilsson, G.; Symons, M. C. R. *J. Chem. Phys.* **1980**, *73*, 4862.
- (15) Samskog, P. O.; Kispert, L. D.; Lund, A. *J. Chem. Phys.* **1983**, *79*, 635.
- (16) Samskog, P. O.; Lund, A. *Chem. Phys. Lett.* **1980**, *75*, 525.
- (17) Sagstuen, E.; Lindgren, M.; Lund, A. *Radiat. Res.* **1991**, *128*, 235.
- (18) Pauwels, E.; Van, Speybroeck, V.; Waroquier, M. *J. Phys. Chem. A* **2006**, *110*, 6504.
- (19) Pauwels, E.; Lahorte, P. G. A.; Vanhaelewyn, G. C. A. M.; Callens, F. J.; De Proft, F. J. A.; Geerlings, P.; Waroquier, M. *J. Phys. Chem. A* **2002**, *106*, 12340.
- (20) Kanters, J. A.; Roelofs, G.; Alblas, B. P.; Meinders, I. *Acta Crystallogr., Sect. B* **1977**, *33*, 665.
- (21) Takagi, S.; Jeffrey, G. A. *Acta Crystallogr., Sect. B* **1997**, *33*, 3510.
- (22) Schonland, D. S. *Proc. Phys. Soc.* **1959**, *73*, 788.
- (23) Nelson, W. H. *J. Magn. Reson.* **1980**, *38*, 71.
- (24) VandeVondele, J.; Krack, M.; Mohamed, F.; Parrinello, M.; Chassaing, T.; Hutter, J. *Comput. Phys. Commun.* **2005**, *167*, 103.
- (25) <http://cp2k.berlios.de>.
- (26) Becke, A. D. *Phys. Rev. A* **1988**, *38*, 3098; Lee, C.; Yang, W.; Parr, R. G. *Phys. Rev. B* **1988**, *37*, 785.
- (27) Lippert, G.; Hutter, J.; Parrinello, M. *Mol. Phys.* **1997**, *92*, 477.
- (28) Goedecker, S.; Teter, M.; Hutter, J. *Phys. Rev. B* **1996**, *54*, 1703; Hartwigsen, C.; Goedecker, S.; Hutter, J. *Phys. Rev. B* **1998**, *58*, 3641.
- (29) VandeVondele, J.; Hutter, J. *J. Chem. Phys.* **2007**, *127*, 114105.
- (30) Declerck, R.; Pauwels, E.; Van, Speybroeck, V.; Waroquier, M. *Phys. Rev. B* **2006**, *74*, 245103.
- (31) Lippert, G.; Hutter, J.; Parrinello, M. *Theor. Chem. Acc.* **1999**, *103*, 124; Krack, M.; Parrinello, M. *Phys. Chem. Chem. Phys.* **2000**, *2*, 2105.
- (32) Godbout, N.; Salahub, D. R.; Andzelm, J.; Wimmer, E. *Can. J. Chem.* **1992**, *70*, 560.
- (33) Declerck, R.; Pauwels, E.; Van Speybroeck, V.; Waroquier, M. *J. Phys. Chem. B*, in press.
- (34) Box, H. C.; Budzinski, E. E.; Potienko, G. *J. Chem. Phys.* **1978**, *69*, 1966.
- (35) Box, H. C.; Budzinski, E. E.; Potienko, G. *J. Chem. Phys.* **1980**, *73* (5), 2052.